Inorg. Chem. **2003**, *42*, 696–708

Inorganic Chemistry
Article

Electronic Structure Contributions to Electron-Transfer Reactivity in Iron–Sulfur Active Sites: 3. Kinetics of Electron Transfer

Pierre Kennepohl and Edward I. Solomon*

Department of Chemistry, Stanford University, Stanford, California 94305-5080

Received May 8, 2002

The kinetics of electron transfer for rubredoxins are examined using density functional methods to determine the electronic structure characteristics that influence and allow for fast electron self-exchange in these electron-transport proteins. Potential energy surfaces for $[FeX_4]^{2-,1-}$ models confirm that the inner-sphere reorganization energy is inherently small for tetrathiolates ($\lambda_i^{ese} \approx 0.1$ eV), as evidenced by the only small changes in the equilibrium Fe–S bond distance during redox ($\Delta r_{redox} \approx 0.05$ Å). It is concluded that electronic relaxation and covalency in the reduced state allow for this small λ_i^{ese} in this case relative to other redox couples, such as the tetrachloride. Using a large computational model to include the protein medium surrounding the $[Fe(SCys)_4]^{2-,1-}$ active site in *Desulfovibrio vulgaris* Rubredoxin, the electronic coupling matrix element for electron self-exchange is defined for direct active-site contact (H_{DA}^0). The simple Beratan–Onuchic model is used to extend coupling over the complete surface of the protein to provide an understanding of probable electron-transfer pathways. Regions of similar coupling properties are grouped together to define a surface coupling map, which reveals that very efficient self-exchange occurs only within 4 σ-bonds of the active site. Longer-range electron transfer cannot support the fast rates of electron self-exchange observed experimentally. Pathways directly through the two surface cysteinate ligands dominate k_{ese}^{∞}, but surface-accessible amides hydrogen-bonded to the cysteinates also contribute significantly to the rate of electron self-exchange.

Introduction

Electron transfer (ET) has been the focus of much interest in the chemical literature.[1−10] In biological systems, ET processes are critical for the proper control of important biochemical pathways. Rubredoxins (Rds) are a well-studied class of small iron−sulfur proteins that function as biological electron-transport agents. Recent work has focused on defining the fundamental electronic structure characteristics of the $[Fe(SCys)_4]^{2-,1-}$ redox couple in Rds and determining its effects on the redox characteristics of these ET proteins.[3,11−22] This is the third paper in a series that addresses

---

* Correspondence should be addressed to this author. Electronic-mail communication is encouraged (edward.solomon@stanford.edu).

(1) Ratner, M. A. *Int. J. Quantum Chem.* **1978**, *14*, 675−694.
(2) Marcus, R. A.; Sutin, N. *Biochim. Biophys. Acta* **1985**, *811*, 265−322.
(3) Holm, R. H.; Kennepohl, P.; Solomon, E. I. *Chem. Rev.* **1996**, *96*, 2239−2314.
(4) Skourtis, S. S.; Beratan, D. *N. J. Biol. Inorg. Chem.* **1997**, 2, 378−386.
(5) Utimoto, K. *New Challenges Org. Electrochem.* **1998**, 279−306.
(6) Mataga, N.; Miyasaka, H. *Adv. Chem. Phys.* **1999**, *107*, 431−496.
(7) Sutin, N. *Adv. Chem. Phys.* **1999**, *106*, 7−33.
(8) Kuznetsov, A. M.; Ulstrup, J. *Electrochim. Acta* **2000**, *45*, 2339−2361.
(9) Moser, C. C.; Page, C. C.; Chen, X.; Dutton, P. L. *Subcell. Biochem.* **2000**, *35*, 1−28.
(10) Bellelli, A.; Brunori, M.; Brzezinski, P.; Wilson, M. T. *Methods (San Diego)* **2001**, *24*, 139−152.
(11) Deaton, J. C.; Gebhard, M. S.; Koch, S. A.; Millar, M.; Solomon, E. I. *J. Am. Chem. Soc.* **1988**, *110*, 6241−6243.
(12) Deaton, J. C.; Gebhard, M. S.; Solomon, E. I. *Inorg. Chem.* **1989**, *28*, 877−889.
(13) Butcher, K. D.; Didziulis, S. V.; Briat, B.; Solomon, E. I. *Inorg. Chem.* **1990**, *29*, 1626−1637.
(14) Butcher, K. D.; Didziulis, S. V.; Briat, B.; Solomon, E. I. *J. Am. Chem. Soc.* **1990**, *112*, 2231−2242.
(15) Butcher, K. D.; Gebhard, M. S.; Solomon, E. I. *Inorg. Chem.* **1990**, *29*, 2067−2074.
(16) Gebhard, M. S.; Deaton, J. C.; Koch, S. A.; Millar, M.; Solomon, E. I. *J. Am. Chem. Soc.* **1990**, *112*, 2217−2231.
(17) Gebhard, M. S.; Koch, S. A.; Millar, M.; Devlin, F. J.; Stephens, P. J.; Solomon, E. I. *J. Am. Chem. Soc.* **1991**, *113*, 1640−1649.
(18) Lowery, M. D.; Guckert, J. A.; Gebhard, M. S.; Solomon, E. I. *J. Am. Chem. Soc.* **1993**, *115*, 3012−3013.
(19) Williams, K. R.; Hedman, B.; Hodgson, K. O.; Solomon, E. I. *Inorg. Chim. Acta* **1997**, *263*, 315−321.
(20) Rose, K.; Shadle, S. E.; Eidsness, M. K.; Kurtz, D. M.; Scott, R. A.; Hedman, B.; Hodgson, K. O.; Solomon, E. I. *J. Am. Chem. Soc.* **1998**, *120*, 10743−10747.
(21) Kennepohl, P.; Solomon, E. I. *Inorg. Chem.* **2003**, *42*, 679−688.
(22) Kennepohl, P.; Solomon, E. I. *Inorg. Chem.* **2003**, *42*, 689−695.

10.1021/ic0203320 CCC: $25.00

the electronic structure contributions to the redox properties of monomeric $[FeX_4]^{2-,1-}$ redox sites.

In part 1, it was determined that *electronic relaxation* results in large changes in the electron density distribution over the complex and stabilizes the oxidized site by massive ligand-to-metal charge transfer (LMCT) upon oxidation.[21] The influence of passive electrons in charge-transfer stabilization of the oxidized site is extremely important, underscoring that this so-called *one-electron* $Fe^{II} \rightarrow Fe^{III}$ redox process is more complex. In part 2, electronic structure contributions to the thermodynamics of electron transfer in $[FeX_4]^{2-,1-}$ systems are discussed, specifically addressing the large observed differences in the redox potentials of $[FeCl_4]^{2-,1-}$ and $[Fe(SR)_4]^{2-,1-}$.[22] A large difference in the lowest vertical ionization energies (i.e., the ionization energies of the redox-active molecular orbitals) of the two reduced species is observed (∼1.4 eV), revealing a large difference in their inherent redox behavior. The primary reason for this difference is the higher covalency of the $[Fe(SR)_4]^{2-}$ species relative to $[FeCl_4]^{2-,1-}$, which lowers its effective charge (Z_{eff}^{Fe}) and destabilizes its empty Fe 3d manifold, thus making the tetrathiolate easier to oxidize. A secondary contribution comes from differences in electronic relaxation between the two species; the tetrathiolate, because of the availability of lower-energy charge-transfer states, better stabilizes the oxidized state through LMCT.[21,22]

This present study evaluates electronic structure contributions to the electron-transfer kinetics in these $[FeX_4]^{2-,1-}$ sites. Within the context of the Marcus–Hush theory of electron transfer, the electronic structure of the redox site directly affects the rate constants of electron self-exchange (k_{ese}) in two ways: (i) the inner-sphere reorganization energy (λ_i) and (ii) the electronic coupling matrix element (H_{DA}).[2] The factors affecting λ_i for $[Fe(SR)_4]$ are defined by comparison to the $[FeCl_4]^{2-,1-}$ redox couple, whose behavior upon redox is quite different. The metal–ligand bond distance changes upon redox (Δr_{redox}) are generally quite small for tetrathiolates (∼0.05 Å)[23] while being large for the tetrachloride (0.11 Å).[24,25] A small Δr_{redox} value is essential for efficient electron transfer because it lowers λ_i [$\propto(\Delta r_{redox})^2$]. It has been suggested that the small Δr_{redox} value observed in Rd is due to the protein structure[26] although most model tetrathiolates also exhibit small values of Δr_{redox}. Using DFT methods, we investigate the potential energy surfaces of the two redox couples; we also determine the influence of electronic relaxation on the geometric changes. The results are compared with photoelectron spectroscopy data[21] to determine the origin of the observed behavior.

H_{DA}^{ese} is also evaluated for these systems using DFT methods and including the effects of electronic relaxation. This is extended to a Rd structural model that includes a large peptide fragment in the vicinity of the active site. This model is used to evaluate the effect of the protein matrix on the electronic structure of the active site. The two cysteinate ligands closest to the surface of the protein, Cys(9) and Cys(42), are quite different from those that are more buried, Cys(6) and Cys(39) (see Figure 1A). This structural asymmetry—with respect to both the orientation of the cysteinates and their involvement in hydrogen bonding—is included in the calculations to determine its influence on the electronic structure and ET properties. Also, using the results from our calculations of H_{DA}^{ese} and λ_i, relative contributions to the rate are estimated and mapped onto the surface of the protein to determine which pathways could reasonably allow for the rapid electron self-exchange that is observed experimentally.[27,28]

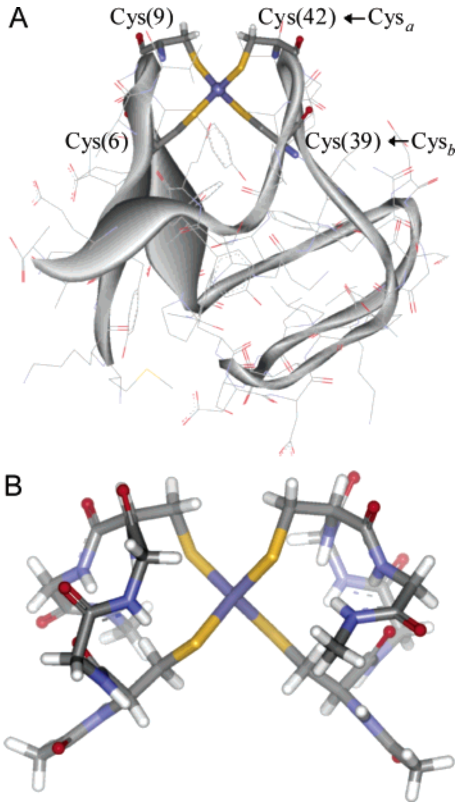

Figure 1. (A) Protein structure of *Dv* Rd (1RB9). The ligands to the Fe at the active site are labeled. Cys(9) and Cys(42) are labeled Cys_a and are nearer the surface of the protein than Cys(6) and Cys(42), which are labeled Cys_b. (B) Computational wild type (CWT) structure used for DFT calculations on the Rd active-site structure. The details of truncation points for the protein structure are given in the text. Importantly, the CWT structure retains the structural and H-bonding asymmetry between Cys_a and Cys_b that occurs in the actual protein structure.

Experimental Section

Density functional theory (DFT) calculations were performed using the commercially available Amsterdam Density Functional (ADF1999 and ADF2000)[29−33] and Gaussian (Gaussian 98)[34] codes. In ADF, the Vosko, Wilke, and Nusair (VWN) local density

---

(23) Bond distances for tetrathiolate are average values for a series of ferrous (CSD: DOKPUO, LAJFUX, PAFVIB, PTHPFE10, VAPVUD, ZAGYIP) and ferric (CSD: BOSTOS, CANCUP, CANDAW, JURHIN, OXYSFEO10) structures.

(24) Evans, D. J.; Hills, A.; Hughes, D. L.; Leigh, G. J. *Acta Crystallogr. C: Cryst. Struct. Commun.* **1990**, *C46*, 1818–1821.

(25) Ferrari, A.; Brainbanti, A.; Bigliardi, G. *Acta Crystallogr.* **1963**, *16*, 846–847.

(26) Sigfridsson, E.; Olsson, M. H. M.; Ryde, U. *J. Phys. Chem. B* **2001**, *105*, 5546–5552.

(27) Im, S. G.; Sykes, A. G. *J. Chem. Soc., Dalton Trans.* **1996**, 2219–2222.

(28) Jensen, T. J.; Gray, H. B.; Ulstrup, J. *J. Inorg. Biochem.* **1999**, *74*, 181–181.

approximation[35] was supplemented with standard nonlocal corrections from Becke[36] and Perdew[37,38] (BP86). All ADF results were obtained using a triple-ζ STO basis set (Basis IV) for the valence levels of all heavy atoms. Core levels were defined for $n = 1$, 2 for Fe and S and for $n = 1$ for all second-row elements. Charge decomposition for the ADF calculations was performed using the built-in Hirshfeld and Mulliken charge analyses. Complementary calculations using the BP86 functional were performed with Gaussian using a 6-311G(d,p) basis set; charge decomposition of these results as performed using AiM2000,[39] a Windows-based Atoms in Molecules[39] charge decomposition program. The two quantum mechanics codes gave similar wave function descriptions. All calculations were performed on either an SGI Origin 2000 8-cpu RO10k server running IRIX 6.5.3 or an Intel dual Pentium III Xeon system running RedHat Linux 7.0. Parallelization of ADF and Gaussian was done using built-in PVM and shared-memory architectures, respectively. Details of specific input parameters used for all published calculations are included as Supporting Information. Comparisons of experimental photoelectron, X-ray absorption, and UV−vis absorption spectra offer a strong database of information for evaluating the strength of the BP86 density functional in providing a good representation of the electronic structure of high-spin Fe(II) and Fe(III) complexes, as well as reasonable geometries. As observed from this and previous studies,[21,22] BP86 is a useful functional for our purposes.

Potential energy surfaces were obtained by using the LINEAR TRANSIT code within ADF. The Fe−L bond distance was varied systematically between 2 and 4.0 Å; all other degrees of freedom were fully optimized. Geometries were optimized under D_{2d} symmetry constraints to maintain the known geometric restrictions of the models. Surfaces for the unrelaxed $[\mathrm{FeCl_4}]^{1-}$ and $[\mathrm{Fe(SCH_3)_4}]^{1-}$ species were obtained by removal of an electron from the redox-active molecular orbital (RAMO, vide infra) of the reduced species and recalculation *without* reconverging the potential. The geometric structure was maintained at each $r_{\mathrm{Fe-L}}$ exactly as it was for the optimized structure in the reduced state.

Protein Structural Models. Geometric data for the reduced and oxidized forms of *Desulfovibrio vulgaris* Rd (*Dv* Rd) were obtained from the Protein Databank (PDB) as structures 1RB9 and 8RXN, respectively. These structures are given to 0.92-Å (1RB9) and 1.00-Å (8RXN) resolution. These structures represent one of only two pairs of Rd structures wherein both redox states have been structurally characterized. The other crystallographically defined redox pair has been obtained for *Pyrococcus furiosis* Rd (*Pf* Rd: 1CAA, 1CAD) to a resolution of ∼1.8 Å. Structural changes upon redox are somewhat larger for the *Pf* Rd structures, but they are still not enough to significantly impact the conclusions drawn from *Dv* Rd. In both cases, structural changes are generally small in the region around the active site. DFT calculations were performed on a truncated structural model of *Dv* Rd; this model is shown in Figure 1B and termed the computational wild type (CWT). The backbone of the active-site double-loop structure includes the Val(5)-Tyr(11) and Val(38)-Ala(44) peptide segments. All noncysteinate side chains are truncated at the C(α) positions and replaced with protons. Terminal residues are completely truncated at their C(α) positions as methyl groups. The cysteinate ligands are included completely in the CWT structural model. Protons are added using MSI Cerius[2] software. The CWT model was investigated in four different geometries: CWT(1RB9), CWT(8RXN), CWT(Opt2), and CWT(Opt3). CWT(1RB9) and CWT(8RXN) are based on the corresponding crystal-structure coordinates. CWT(Opt2) and CWT(Opt3) were partially optimized in the ferrous and ferric states, respectively, to energy gradients of 10^{-5} au using CWT(1RB9) as a starting geometry. The truncation points for the model were fixed in Cartesian space to maintain constraints usually provided by the rest of the protein structure. These optimized geometries were in good agreement with the crystallographic structures. Full optimizations (not reported) converged to largely different geometric structures through the creation of hydrogen-bonding interactions between protein residues that could not be formed in the full protein structure.

To evaluate the influence of hydrogen bonding on the active site, a computational model that lacked these interactions was also defined. The computational enamine mutant (CEM) structure is identical to the CWT structure, except that all backbone amides (O═C−NH) that H-bond to the cysteinate ligands are tautomerized into their complementary enamines (HO−C═N). This simple modification removes all direct interactions through the amide hydrogens while maintaining the basic geometric structure of the surrounding matrix.

Results and Analysis

Reorganization Energy. Potential energy surfaces [$V(r)$, Figure 2] were calculated for $[\mathrm{FeCl_4}]^{2-,1-}$ and $[\mathrm{Fe(SCH_3)_4}]^{2-,1-}$ using the BP86 density functional. The open circles represent DFT-calculated fixed-geometry points for the reduced $V_{\mathrm{Fe^{II}}}(r)$ state, the relaxed oxidized $V_{\mathrm{Fe^{III}}}(r)$ state, and an unrelaxed oxidized $V_{\mathrm{Fe^{III*}}}(r)$ state. Each of these $V(r)$ surfaces was fit to a Morse-type function (eq 1, solid lines in Figure 2); this functional form gave good fits to the calculated energies in all three cases. The surfaces are therefore described in terms of r_e (equilibrium bond distance), D_e (depth of the potential well), and β (decay at long distances). The fit results for each $V(r)$ are given in Table 1.

$$V(r) = V(r_e) + D_e(1 - e^{-\beta(r-r_e)})^2 \qquad (1)$$

The ferrous potential energy surfaces [$V_{\mathrm{Fe^{II}}}(r)$] for the two species are remarkably similar in both their overall shapes (D_e and β) and their calculated equilibrium bond distances (r_e). The calculated r_e values for $[\mathrm{FeCl_4}]^{2-}$ and $[\mathrm{Fe(SCH_3)_4}]^{2-}$

---

(29) Te Velde, G.; Bickelhaupt, F. M.; Baerends, E. J.; Fonseca Guerra, C.; van Gisbergen, S. J. A.; Snijders, J. G.; Ziegler, T. *J. Comput. Chem.* **2001**, *22*, 931−967.

(30) Versluis, L.; Ziegler, T. *J. Chem. Phys.* **1988**, *88*, 322−328.

(31) Baerends, E. J.; Ellis, D. E.; Ros, P. *Chem. Phys.* **1973**, *2*, 41−51.

(32) Te Velde, G.; Baerends, E. J. *J. Comput. Phys.* **1992**, *99*, 84−98.

(33) Guerra, C. F.; Snijders, J. G.; Te Velde, G.; Baerends, E. J. *Theor. Chem. Acc.* **1998**, *99*, 391−403.

(34) Frisch, M. J.; Trucks, G. W.; Schlegel, H. B.; Scuseria, G. E.; Robb, M. A.; Cheeseman, J. R.; Zakrzewski, V. G.; Montgomery, J. A., Jr.; Stratmann, R. E.; Burant, J. C.; Dapprich, S.; Millam, J. M.; Daniels, A. D.; Kudin, K. N.; Strain, M. C.; Farkas, O.; Tomasi, J.; Barone, V.; Cossi, M.; Cammi, R.; Mennucci, B.; Pomelli, C.; Adamo, C.; Clifford, S.; Ochterski, J.; Petersson, G. A.; Ayala, P. Y.; Cui, Q.; Morokuma, K.; Salvador, P.; Dannenberg, J. J.; Malick, D. K.;, Rabuck, A. D.; Raghavachari, K.; Foresman, J. B.; Cioslowski, J.; Ortiz, J. V.; Baboul, A. G.; Stefanov, B. B.; Liu, G.; Liashenko, A.; Piskorz, P.; Komaromi, I.; Gomperts, R.; Martin, R. L.; Fox, D. J.; Keith, T.; Al-Laham, M. A.; Peng, C. Y.; Nanayakkara, A.; Challacombe, M.; Gill, P. M. W.; Johnson, B.; Chen, W.; Wong, M. W.; Andres, J. L.; Gonzalez, C.; Head-Gordon, M.; Replogle, E. S.; Pople, J. A. *Gaussian 98*, revision A.lx; Gaussian, Inc.: Pittsburgh, PA, 2001.

(35) Vosko, S. H.; Wilk, L.; Nusair, M. *Can. J. Phys.* **1980**, *58*, 1200−1211.

(36) Becke, A. D. *Phys. Rev. A: Gen. Phys.* **1988**, *38*, 3098−3100.

(37) Perdew, J. P.; Burke, K.; Emzerhof, M. *ACS Symp. Ser.* **1996**, *629*, 453−462.

(38) Perdew, J. P. *Phys. Rev. B: Condens. Matter* **1986**, *33*, 8822.

(39) Bader, R. F. W. *Atoms in Molecules: A Quantum Theory*; Oxford University Press: New York, 1994.

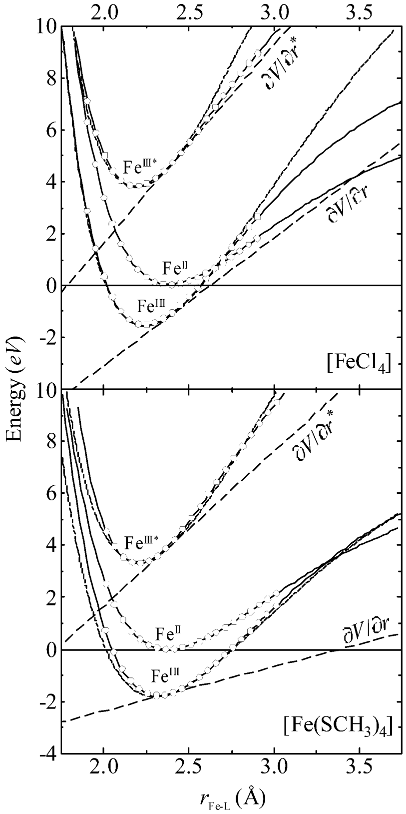

Figure 2. Potential energy surfaces for $[FeCl_4]^{2-,1-}$ and $[Fe(SCH_3)_4]^{2-,1-}$. Open circles correspond to DFT-calculated points along the Fe−L degree of freedom. Solid curves represent Morse potential fits to the calculated surfaces. The minima for each Morse potential provide the calculated equilibrium Fe−L bond distances in each oxidation state. Dotted curves for Fe^{III} and Fe^{III*} are the best-fit curves from applying a linear distorting force ($\partial V/\partial r$) to the Morse function for Fe^{II}. The applied $\partial V/\partial r$ curves for each ferric function are shown as dashed lines. The Fe^{III*} potential energy surface is a theoretical construct that allows for the investigation of the effects of electronic relaxation on the energy landscape during redox.

are also in reasonable agreement with crystallographic data (see Table 1); they are somewhat larger than the experimental bond distances (r_{exp}) but within the deviations generally observed for DFT geometries of transition metal complexes.[40] By contrast, the ferric surfaces [$V_{\text{Fe}^{\text{III}}}(r)$] for the two species are quite different from each other: D_e and β are much larger for $[FeCl_4]^{1-}$, whereas r_e is significantly shorter (by 0.07 Å).

The $V_{\text{Fe}^{\text{II}}}(r) \rightarrow V_{\text{Fe}^{\text{III}}}(r)$ oxidation processes for the two species are thus quite different, especially with respect to the bond distance changes upon redox: $\Delta r_{\text{redox}} = 0.14$ Å for $[FeCl_4]^{2-,1-}$, whereas it is only 0.05 Å for $[Fe(SCH_3)_4]^{2-,1-}$. Experimental bond distance changes upon redox also follow the same trend (Δr_{exp} in Table 1), with much smaller changes in the tetrathiolate than in the tetrachloride redox couple. These differences translate into significant differences in the inner-sphere reorganization energies for electron self-exchange calculated from $V_{\text{Fe}^{\text{II}}}(r) \rightarrow V_{\text{Fe}^{\text{III}}}(r)$ (λ_i^{ese} in Table 1): λ_i^{ese} for the tetrathiolate is very small at 0.12 eV, whereas it is much larger (0.77 eV) for the tetrachloride. Using Δr_{exp} values and Fe−X bond stretching frequencies, λ_i^{ese} is estimated to be 0.3 and 0.7 eV for $[Fe(SR)_4]^{1-}$ and $[FeCl_4]^{1-}$, respectively. The DFT results somewhat underestimate λ_i^{ese} for $[Fe(SR)_4]^{2-,1-}$ relative to the experimentally derived value. However, the calculated results clearly reproduce the significant differences between the two redox couples in both Δr_{redox} and λ_i^{ese}.

Table 1. Best-Fit Parameters for Morse-type Functions for $V(r)^a$

potential energy surface		$V(r_e)$ (eV)	D_e (eV)	β (Å^{-1})	r_e (Å)	Δr_{redox} (Å)	λ_i^{ese} (eV)	r_{exp} (Å)	Δr_{redox} (Å)
		$V(r)$ best fit						experimental	
[FeC1$_4$]	Fe^{II}	0.00	6.80	1.39	2.38	–	–	2.29	–
	Fe^{III*}	3.78	11.75	1.51	2.18	0.20	1.67	–	–
	Fe^{III}	−1.56	11.01	1.44	2.24	0.14	0.77	2.18	0.11
[Fe(SR)$_4$]	Fe^{II}	0.00	6.79	1.30	2.36	–	–	2.33	
	Fe^{III*}	3.31	12.69	1.48	2.19	0.17	0.92	–	–
	Fe^{III}	−1.80	9.92	1.30	2.31	0.05	0.12	2.27	0.06

[a] Experimental parameters derived from Cambridge Structural Database (CSD). Bond distances for tetrathiolate are average values for a series of ferrous (CSD: DOKPUO, LAJFUX, PAFVIB, PTHPFE10, VAPVUD, ZAGYIP) and ferric (CSD: BOSTOS, CANCUP, CANDAW, JURHIN, OXYSFE10) structures.

Fe 2p$_{3/2}$ core ionization energies reflect the effective nuclear charge at the central metal ion ($Z_{\text{eff}}^{\text{Fe}}$) and provide experimental insight into the differences observed above.[21,22] There is a significant difference between the relaxation-corrected Fe 2p$_{3/2}$ binding energies ($E_b^{\text{Fe 2p}_{3/2}}$) for $[FeCl_4]^{2-,1-}$ and $[Fe(SR)_4]^{2-,1-}$; these energies were determined in part 1 and are reproduced in Table 2. In the reduced state, $E_b^{\text{Fe 2p}_{3/2}}$ for the tetrachloride is 1.4 eV greater than that for the tetrathiolate, indicating that $Z_{\text{eff}}^{\text{Fe}}$ is much greater in $[FeCl_4]^{2-}$. DFT-calculated Hirshfeld (Hrf, $Z_{\text{eff}}^{\text{Hrf}}$) and Atoms in Molecules (AIM, $Z_{\text{eff}}^{\text{AIM}}$) charges also support this conclusion (Table 2). More importantly, the changes in $E_b^{\text{Fe 2p}_{3/2}}$ upon oxidation are very different for the two redox couples: $\Delta(E_b^{\text{Fe 2p}_{3/2}})_{\text{redox}} = 2.8$ eV for $[FeCl_4]^{2-,1-}$, whereas it is only 0.4 eV for $[Fe(SR)_4]^{2-,1-}$. These results indicate that, although the charge on the metal changes significantly upon oxidation for the tetrachloride, it changes very little for the tetrathiolate. Again, DFT results correlate well with these experimental observations. The AIM decomposition provides the best correlation between the calculated effective charges for a site and its experimental binding energy, as shown in Figure 3. The correlation between $Z_{\text{eff}}^{\text{AIM}}$ and $E_b^{\text{Fe 2p}_{3/2}}$ fits quite well with the theoretically predicted behavior[41] (solid line, Figure 3), where $E_b^{\text{Fe 2p}_{3/2}} \propto Z_{\text{eff}}{}^2$. From this result, $\Delta q_{\text{redox}}^{\text{Fe 2p}}$ ($\Delta q_{\text{redox}} = Z_{\text{eff}}^{\text{Fe(II)}} - Z_{\text{eff}}^{\text{Fe(III)}}$) is defined for each redox couple and gives good agreement with the results obtained from AIM and Hrf ($\Delta q_{\text{redox}}^{\text{AIM,Hrf}}$), as shown in Table 2. The VBCI analysis in part 1[21] can also be used to independently determine the change in charge upon oxidation ($\Delta q_{\text{redox}}^{\text{VBCI}}$, Table 2). All of these methods of determining Δq_{redox} provide a consistent picture: whereas the change in charge upon redox is quite large for $[FeCl_4]^{2-,1-}$ ($\Delta q_{\text{redox}} \approx 0.2\bar{e}$), it is much smaller for $[Fe(SR)_4]^{2-,1-}$ ($\Delta q_{\text{redox}} \approx 0.1\bar{e}$). This difference in Δq_{redox} between the two redox couples correlates directly with Δr_{redox} (vide supra), which is larger for

---

(40) The negative charge of these complexes in the gas phase contributes to the overestimate of the Fe-X bond distances. The deviation is larger for the tetrachloride, which is unsurprising because of the poorer charge distribution in this complex relative to the tetrathiolate.

(41) Robertson, N. E.; Hidalgo, G. R. *J. Chem. Inf. Comput. Sci.* **1997**, *37*, 458−459.

Table 2. Experimental^a and DFT-Calculated^b Effective Charges

system		PES			DFT/AIM		DFT/Hirshfeld	
		$E_b^{\mathrm{Fe\ 2p}}$	$\Delta q_{\mathrm{redox}}^{\mathrm{Fe\ 2p}}$	$\Delta q_{\mathrm{redox}}^{\mathrm{VBCI}}$	$Z_{\mathrm{eff}}^{\mathrm{AIM}}$	$\Delta q_{\mathrm{redox}}^{\mathrm{AIM}}$	$Z_{\mathrm{eff}}^{\mathrm{Hrf}}$	$\Delta q_{\mathrm{redox}}^{\mathrm{Hrf}}$
$[FeCl_4]$	Fe^{II}	710.8	–	–	1.19	–	1.98	–
	Fe^{II*}	–	–	0.97	2.09	0.90	2.80	0.82
	Fe^{III}	713.6	0.27	0.28	1.37	0.18	2.22	0.24
$[Fe(SCH_3)_4]$	Fe^{II}	709.4	–	–	0.86	–	1.78	–
	Fe^{III*}	–	–	0.92	1.73	0.87	2.55	0.77
	Fe	709.7	0.04	0.16	0.97	0.11	1.90	0.12

^{a} Experimental changes in charge were derived from the ferrous and ferric core Fe $2p_{3/2}$ binding energies ($\Delta q_{\mathrm{redox}}^{\mathrm{Fe\ 2p}}$) from part 2[22] and the VBCI model ($\Delta q_{\mathrm{redox}}^{\mathrm{VBCI}}$) derived in part 1.[21] ^{b} Effective charges were also determined using the Atoms in Molecules ($Z_{\mathrm{eff}}^{\mathrm{AIM}}$) and the Hirshfeld ($Z_{\mathrm{eff}}^{\mathrm{Hrf}}$) charge decomposition of our DFT results for the reduced (Fe^{II}), unrelaxed ferric (Fe^{III*}), and relaxed ferric (Fe^{III}) species. The change in charge upon redox ($\Delta q_{\mathrm{redox}}^{\mathrm{AIM,Hrf}}$) is also determined for oxidation with ($F^{II} \rightarrow Fe^{III}$) and without electronic relaxation ($Fe^{II} \rightarrow Fe^{III*}$).

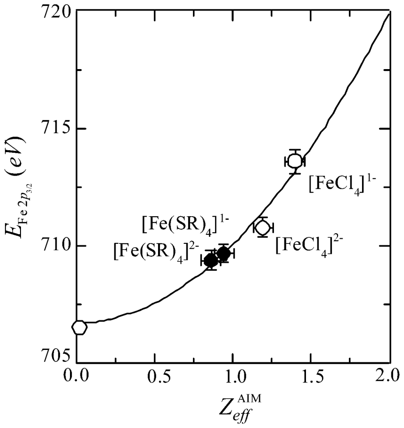

Figure 3. Effective charge versus Fe 2p binding energy.

$[FeCl_4]^{2-,1-}$. This correlation is unsurprising as the electrostatic attraction between the positive metal ion and the negative ligands contributes to the bond length and its increase upon oxidation should correlate with $\Delta r_{\mathrm{redox}}$.

The differences in $\Delta q_{\mathrm{redox}}$ between the two redox couples result from two contributions. First, the change in charge upon redox in the absence of relaxation ($\Delta q_{\mathrm{redox}}^{*} = Z_{\mathrm{eff}}^{\mathrm{FeIII*}} - Z_{\mathrm{eff}}^{\mathrm{FeII}}$) is different in the two redox couples. From Table 2, $\Delta q_{\mathrm{redox}}^{*}$ for $[FeCl_4]^{2-,1-}$ is higher than that for $[Fe(SR)_4]^{2-,1-}$; the more localized valence ionization in the tetrachloride corresponds with its lower covalency relative to the tetrathiolate. Second, as determined in part 1, electronic relaxation has a significant effect on the electron density at the metal center in the final oxidized state. The charge redistribution due to ligand-to-metal charge transfer after oxidation (Δq_{rlx}) was evaluated both theoretically and experimentally for both systems, giving $\Delta q_{\mathrm{rlx}} \approx -0.70\bar{e}$ for $[FeCl_4]^{2-,1-}$ and $\Delta q_{\mathrm{rlx}} \approx -0.75\bar{e}$ for $[Fe(SR)_4]^{2-,1-}$.[21] The overall change in charge for the oxidation process is the sum of Δq_{rlx} and $\Delta q_{\mathrm{redox}}^{*}$. As a result, both the initial-state electronic structure ($0.92\bar{e}$ vs $0.85\bar{e}$) and electronic relaxation ($-0.70\bar{e}$ vs $-0.75\bar{e}$) each contribute $\sim 0.05\bar{e}$; thus, the overall $\Delta q_{\mathrm{redox}}$ of the tetrathiolate redox couple is lower than that of the tetrachloride by $\sim 0.1\bar{e}$ (vide supra).

The relationship between $\Delta q_{\mathrm{redox}}$ and $\Delta r_{\mathrm{redox}}$ can be quantitatively evaluated using the potential energy surfaces developed in Figure 2. Visually, electronic relaxation has a strong influence on the surfaces, as evidenced by the dramatic difference between $V_{\mathrm{Fe^{III}}}(r)$ and $V_{\mathrm{Fe^{III*}}}(r)$ for each redox couple. To investigate these differences, the ferric surfaces are redefined with respect to the $V_{\mathrm{Fe^{III}}}(r)$ surface. A linear distorting force ($\partial V/\partial r$) is applied as a perturbation to shift $V_{\mathrm{Fe^{II}}}(r)$ to generate $V'_{\mathrm{Fe^{III}}}(r)$ and $V'_{\mathrm{Fe^{III*}}}(r)$, which are the best fits to the ferric surfaces using eq 2. The dotted lines in Figure 2 represent $V'_{\mathrm{Fe^{III}}}(r)$ and $V'_{\mathrm{Fe^{III*}}}(r)$ for the two redox couples. The best-fit values for $\partial V/\partial r$ are given in Table 3. An energy shift (b) is necessary to allow for distance-independent shifts in the ferric potential energy surfaces (due to the loss of an electron from the system).

Table 3. Linear Distorting Force ($\partial V/\partial r$) Acting on the Initial Potential Energy Surface upon Ionization^a

system		Z_{eff}		$V'(r)$		point-charge model^b
		Fe	X	$\partial V/\partial r$	b	$\partial V/\partial r$
$[FeCl_4]$	Fe^{III*}	1.99	−0.75	7.56	−12.85	6.46
	Fe^{III}	1.41	−0.62	4.89	−13.48	2.06
$[Fe(SCH_3)_4]$	Fe^{III*}	1.66	−0.63	5.99	−5.83	4.90
	Fe^{III}	0.99	−0.44	1.74	−10.14	0.37

^{a} Data given for the distortion $[(\partial V/\partial r)r + b]$ necessary to yield $V'(r)$ both including (Fe^{III}) and excluding (Fe^{III*}) electronic relaxation. ^{b} Parameters calculated using the point-charge model were determined using the DFT-optimized D_{2d} geometries and the effective atomic charges (Z_{eff}) obtained from Atoms in Molecules (AIM) analysis of the BP86 densities.

$$V'_{\mathrm{Fe^{III}}}(r) = V_{\mathrm{Fe^{II}}}(r) + (\partial V/\partial r)r + b \qquad (2)$$

As expected, surfaces generated by assuming such a linear distortion on the ferrous surface are very good near the equilibrium bond distance but quite poor at large deviations from equilibrium; because the region of interest is near r_e, these deviations are not significant in this analysis. In the absence of relaxation, $\partial V/\partial r$ is very large for both $[FeCl_4]^{2-,1-}$ (7.56 eV/Å) and $[Fe(SCH_3)_4]^{2-,1-}$ (5.99 eV/Å), although it is larger for the former. This finding is in agreement with the differences in $\Delta q_{\mathrm{redox}}^{*}$ discussed previously; there is an inherent difference between the ferrous complexes that results in a larger distorting force upon oxidation in the tetrachloride. The dominant factor in determining the magnitude of this distorting force without electronic relaxation is the metal character of the RAMO, i.e., its covalency. These large $\partial V/\partial r$ values result in dramatic bond shortening upon ionization in both unrelaxed systems: $\Delta r_{\mathrm{redox}}^{*} = 0.20$ Å for $[FeCl_4]^{2-,1-}$ and 0.17 Å for $[Fe(SCH_3)_4]^{2-,1-}$. It is somewhat surprising that the large difference in $\partial V/\partial r$ between the two unrelaxed systems results in only a mild difference in $\Delta r_{\mathrm{redox}}^{*}$, but the anharmonicity of the potentials (from nuclear repulsion at short distances) dampens the effect of such large $\partial V/\partial r$ values and minimizes the resultant Δr_{redox}.[42]

The potential energy surfaces change dramatically when electronic relaxation is included (see Figure 2). For both redox couples, $\partial V/\partial r$ is much lower with electronic relaxation: the distorting force decreases to 4.9 eV/Å for $[\text{FeCl}_4]^{1-}$ and to 1.7 eV/Å for $[\text{Fe(SCH}_3)_4]^{1-}$. The greatest difference between the unrelaxed and relaxed ferric systems is the charge redistribution, which decreases the positive charge at the metal center (and also the negative charge on the ligands) in the relaxed state; this minimizes the electrostatic attraction with the anionic ligands and decreases the force for contraction of the metal−ligand bonds. An estimate of $\partial V/\partial r$ based solely on the Coulombic forces that would act on each system is included in Table 3. The results from this point-charge model are quite similar to those for the potential energy surfaces and strengthens the conclusion that electronic relaxation lowers $\partial V/\partial r$ in both $[\text{FeCl}_4]^{2-,1-}$ and $[\text{Fe(SCH}_3)_4]^{2-,1-}$, resulting in a smaller Δr_{redox} in both redox couples. The most important consequence of lowering $\partial V/\partial r$ through relaxation is its effect on the inner-sphere reorganization energy ($\lambda_{\text{i}}^{\text{ese}}$). The decrease in the distorting force due to electronic relaxation lowers Δr_{redox} by 0.06 Å for $[\text{FeCl}_4]^{2-,1-}$ and by 0.12 Å for $[\text{Fe(SCH}_3)_4]^{2-,1-}$; the effect is large in both redox couples but somewhat larger for the tetrathiolate. The effect on the reorganization energy is also considerable; the inclusion of electronic relaxation decreases $\lambda_{\text{e}}^{\text{se}}$ by nearly 1 eV in both cases (see Table 1). Because $\lambda_{\text{i}}^{\text{ese}}$ without relaxation is much larger for $[\text{FeCl}_4]^{2-,1-}$ than for $[\text{Fe(SCH}_3)_4]^{2-,1-}$, $\lambda_{\text{i}}^{\text{ese}}$ is still quite large after relaxation for $[\text{FeCl}_4]^{2-,1-}$ (0.77 eV), whereas that for $[\text{Fe(SCH}_3)_4]^{2-,1-}$ is small (0.12 eV).

Electronic Coupling. The one-electron coupling matrix elements for electron self-exchange (H'^{0}_{DA}) of $[\text{FeCl}_4]^{2-,1-}$, $[\text{Fe(SCH}_3)_4]^{2-,1-}$, and *Pf* Rd are calculated using the formalism developed by Newton and co-workers,[43−49] which applies McConnell's superexchange model for ET and correlates ligand contributions to the redox-active molecular orbital (RAMO) with the magnitude of H'^{0}_{DA}. For the *Pf* Rd redox site, it is necessary to describe and evaluate the overall active-site electronic structure to define differences between the protein active site and the model system and to determine the ligand terms to include in the analysis.

Table 4. Active-Site Geometric Parameters for All CWT Structural Models

		8RXN	1RB9	Δr_{redox}	Opt3	Opt2	Δx_{redox}
r_{FeS}	$\text{Cys}_{\text{a(avg)}}$	2.26	2.26	0.00	2.27	2.30	+0.03
	$\text{Cys}_{\text{b(avg)}}$	2.29	2.29	0.00	2.33	2.36	+0.03
$r_{\text{N(H)−S}}$	$\text{Cys}_{\text{a(avg)}}$	3.48	3.46	−0.02	3.49	3.39	−0.10
	$\text{Cys}_{\text{b(1)}}$	3.55	3.55	0.00	3.47	3.37	−0.10
	$\text{Cys}_{\text{b(2)}}$	3.59	3.60	+0.01	3.61	3.64	+0.03
a_{FeSC}	$\text{Cys}_{\text{a(avg)}}$	111.2	108.4	−2.8	109.7	113.2	+3.5
	$\text{Cys}_{\text{b(avg)}}$	101.4	100.7	−0.7	103.0	101.6	−1.4
d_{FeSCC}	$\text{Cys}_{\text{a(avg)}}$	89.2	92.0	+2.8	86.5	83.8	−2.7
	$\text{Cys}_{\text{b(avg)}}$	173.6	173.9	+0.3	171.3	172.0	+0.7
$a_{\text{S}_x\text{FeS}_y}$	$x = y$	110.1	110.6	+0.5	111.5	112.9	+1.4
	$x \neq y$	113.3	114.4	+1.1	113.7	113.3	−0.4

Geometric and Electronic Structure of $[\text{Fe(SCys)}_4]^{2-,1-}$ in Rd. DFT calculations were performed on the CWT structure (Figure 1B) using the reduced (1RB9) and oxidized (8RXN) crystallographic coordinates, as well as on partially optimized structures in both the reduced (Opt-Red) and oxidized (Opt-Ox) states. The two Cys_{a} and Cys_{b} cysteinate ligands (see Figure 1A) that comprise the active site of Rd are structurally quite different from each other with respect to their interaction with the iron site and their location within the protein structure, as seen from Table 4. Structurally, CWT(Opt-Red) and CWT(Opt-Ox) are similar to the crystallographic data, with a heavy-atom average standard deviation of ~0.2 Å between Opt-Red/1RB9 and between Opt-Ox/8RXN. Unsurprisingly, surface-exposed backbone amide groups deviate most strongly from the crystallographic data. The Opt-Red and Opt-Ox geometries are used because they provide reasonable structural information for both the heavy atoms and the protons and their interactions (such as H-bonding) with the heavy atoms in CWT.

CWT(Opt-Red) and CWT(Opt-Ox) offer an opportunity to investigate the importance of (Cys)S···HN(amide) interactions and their effect on the active site. The NH bond distances (r_{NH}) reflect the relative strength of NH···D interactions with potential donors (D); a stronger H-bond will weaken (and lengthen) the NH bond. Noninteracting amide groups within the CWT model are used as an internal reference for these comparisons (Table 5). In CWT(Opt-Ox), all amide NH groups involved in H-bonds have r_{NH} ~0.005 Å greater than free amide NH groups. The free NH groups, and those involved in protein-based H-bonds, decrease slightly ($\Delta r_{\text{NH}} \approx -0.002$ Å) upon reduction to the CWT(Opt-Red) structure. By contrast, the r_{NH} value for amides involved in NH···S(Cys) interactions *increases upon reduction*, indicating that the H-bonds to the active-site cysteinates are stronger in the reduced state. However, the redox process affects specific active-site H-bonds differently. Each Cys_{a} has only one H-bond, which increases significantly in strength upon reduction; r_{NH} elongation ($\Delta r_{\text{NH}} \approx +0.010$ Å) is accompanied by a large decrease in the NH−S distance ($\Delta r_{\text{NH−S}} \approx -0.12$ Å). Each Cys_{b} has two H-bonds, each of which behaves quite differently upon redox. One of the H-bonds behaves similarly to the H-bond to Cys_{a} ($\Delta r_{\text{NH}} \approx +0.010$ Å and $\Delta r_{\text{NH−S}} \approx -0.11$ Å), indicating a significant increase in the strength of that H-bond upon reduction. The other Cys_{b} H-bond is far less affected by the redox process ($\Delta r_{\text{NH}} \approx +0.005$ Å and $\Delta r_{\text{NH−S}} \approx -0.02$ Å). The secondary

---

(42) The relationship between the distorting force and the bond changes upon oxidation for the Morse-type potential is compared to that occurring in a harmonic field in the Supporting Information. The linear relationship in a harmonic field is dampened by the anharmonicity in the Morse potential; this deviation increases as the distorting force increases.

(43) Newton, M. D.; Ohta, K.; Zhong, *E. J. Phys. Chem.* **1991**, *95*, 2317−2326.

(44) Newton, M. D. *Int. J. Quantum Chem.* **2000**, *77*, 255−263.

(45) Newton, M. D. *Jerusalem Symp. Quantum Chem. Biochem.* **1986**, *19*, 305−314.

(46) Newton, M. D. *Jerusalem Symp. Quantum Chem. Biochem.* **1990**, *22*, 157−170.

(47) Newton, M. D. *J. Phys. Chem.* **1988**, *92*, 3049−3056.

(48) Newton, M. D. *J. Phys. Chem.* **1986**, *90*, 3734−3739.

(49) Liang, C. X.; Newton, M. D. *J. Phys. Chem.* **1992**, *96*, 2855−2866.

Table 5. Geometric Parameters Used to Define Extent of Hydrogen-Bonding in CWT(Opt2) and CWT(Opt3)

backbone NH group	H-bond donor	Opt3			Opt2			redox		
		r_{NH}	r_{FeS}	r_{NH-S}	r_{NH}	r_{FeS}	r_{NH-S}	Δr_{NH}	Δr_{FeS}	Δr_{NH-S}
					Loop 1					
Cys(6)	−	1.027	2.337		1.025	2.356		−0.002	+0.019	
Thr(7)	−	1.025			1.024			−0.001		
Val(8) S	Cys(6)	1.032		2.49	1.041		2.37	+0.009	−0.08	
Cys(9) S	Cys(6)	1.034	2.272	2.53	1.038	2.308	2.58	+0.004	+0.036	+0.05
Gly(10) OCN	Cys(6)	1.030			1.028			−0.002		
Tyr(11) S	Cys(9)	1.031		2.55	1.042		2.40	+0.009		−0.15
					Loop 2					
Cys(39)	−	1.028	2.325		1.027	2.359		−0.001	+0.034	
Pro(40)	−	1.025			1.023			−0.002		
Val(41) S	Cys(39)	1.033		2.49	1.044		2.36	+0.011		−0.13
Cys(42) S	Cys(39)	1.033	2.271	2.64	1.038	2.299	2.57	+0.005	+0.028	−0.07
Gly(43) OCN	Cys(39)	1.032			1.030			−0.002		
Ala(44) S	Cys(42)	1.032		2.49	1.042		2.39	+0.010		−0.10

Table 6. Description of RAMO

contributions		Fe^{II} HOMO					Fe^{III} LUMO			
		SCH_3	1RB9	8RXN	Opt2	CEM	SCH_3	1RB9	8RXN	Opt3
					RAMO					
Fe	3d	83.1	84.7	84.5	86.1	79.3	82.0	84.8	84.6	85.2
	4s/p	1.2	0.9	1.0	1.6	1.5	1.4	0.8	0.8	1.4
Cys_a	SC_{π}^{σ}	1.4	1.5	1.6	1.2	1.5	1.6	1.6	1.6	1.4
	$S_{p\sigma}^{\pi}$	0.6	0.7	0.6	0.7	0.8	0.9	0.9	1.0	0.8
Cys_b	SC_{π}^{σ}	−	1.2	1.2	0.8	0.9	−	1.1	1.1	1.0
	R_{total}	1.7	0.7	1.0	0.7	6.8	0.2	0.8	1.1	0.8
	Fe	3.40	3.35	3.36	3.41	3.32	3.67	3.70	3.70	3.73
					ρ_{spin}					
S		0.15	0.15	0.15	0.14	0.16	0.31	0.30	0.30	0.29
R		0.03	0.05	0.06	0.05	0.02	0.02	0.10	0.12	0.12
					Z_{eff}^{Hrf}					
Fe		1.78	1.71	1.71	1.69	1.71	1.90	1.81	1.81	1.80
S		−0.90	−0.81	−0.80	−0.78	−0.81	−0.78	−0.71	−0.71	−0.70

H-bond interaction is not optimal for good overlap because of its poorer orientation relative to the sulfur atom.

The overall electronic behavior of the Rd active-site model is quite similar to that observed in small-molecule $[Fe(SR)_4]^{2-,1-}$ systems. Previous experimental and DFT studies on the electronic structure of the $[Fe(SR)_4]^{2-,1-}$ active site have allowed for a detailed description of the electronic changes that occur upon ionization. The largest change upon oxidation is a dramatic increase in spin polarization that causes inversion of the bonding description of the ferric site.[13,14,21] This inversion occurs in the majority α-spin orbitals, where ligand-based orbitals become the highest occupied and the filled Fe 3d manifold is driven below the valence S 3p manifold. The effect of this inversion on the Fe−S bonding is, however, relatively limited because it has little effect on the minority β-spin orbitals, which are dominantly responsible for the metal−ligand bonding. The largest effect in the β-spin orbitals is a lowering of the Fe 3d manifold, increasing covalency through better energy matching with the S 3p manifold. The increased ligand-to-metal charge transfer (LMCT) in the oxidized state is the mechanism for electronic relaxation (as shown in part 1) and is responsible for significant stabilization of the oxidized state. There are a number of small differences between the CWT(Opt-Red/Opt-Ox) and $[Fe(SCH_3)_4]^{2-,1-}$ structures, particularly the orientation of the cysteinates and the presence of H-bonds to the sulfurs (vide supra). To isolate H-bonding effects from other structural differences (e.g., thiolate orientation) between CWT and $[Fe(SCH_3)_4]^{2-,1-}$, the CEM structure (with enamines rather than amides) was constructed as an intermediate between the limiting structures. The spin density distribution (ρ_{spin} in Table 6) provides a way to compare the overall differences in the electronic structures of the reduced sites in the CEM and CWT structures. The presence of the hydrogen bonds (in going from CEM → CWT) results in a decrease in the metal−ligand covalency and an increase in the spin density on the amides that are H-bonded to the active site. The decrease in covalency (from 83% Fe character in CEM to 86% in CWT according to ρ_{spin}) is consistent with S K-edge XAS results[20] and reflects a decrease in the donor strength of the thiolate ligands as a result of the hydrogen-bonding interactions.

The nature of the RAMO is of fundamental importance in defining the one-electron redox process. The RAMO is the highest-occupied molecular orbital (HOMO) of the reduced species and the lowest-unoccupied molecular orbital (LUMO) of the oxidized species, which should be identical in a one-electron process (i.e., without electronic relaxation). Table 6 gives the complete description of the RAMO in terms of its component atomic orbitals in both oxidation states for the different CWT structures; a visual representation of the RAMO is also provided in Figure 4. The RAMO is surprisingly robust to the geometry of the active site and differs only slightly between the two oxidation states. It is

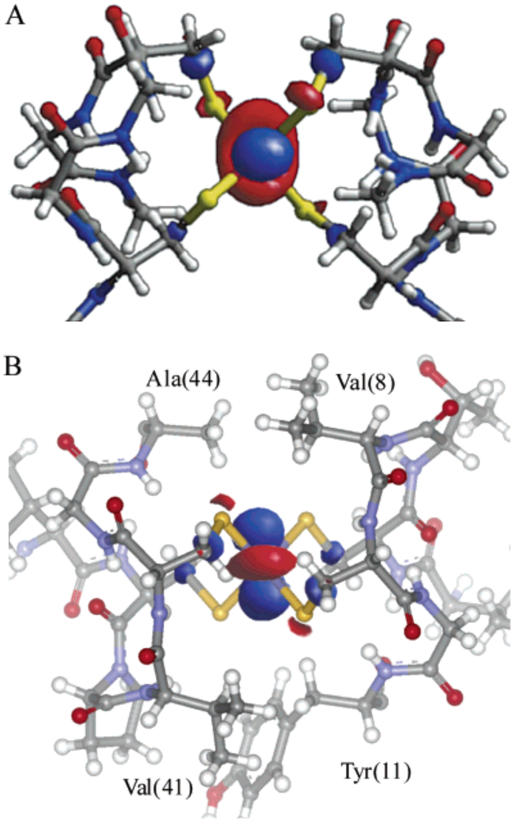

Figure 4. Redox-active molecular orbital for CWT(1RB9) in the reduced state in two orientations. The main component of the RAMO (Fe 3d$_{z^2}$) points along the direction of the closest surface of the protein; it is therefore not well oriented for direct overlap with a redox partner at the surface of the protein.

Scheme 1

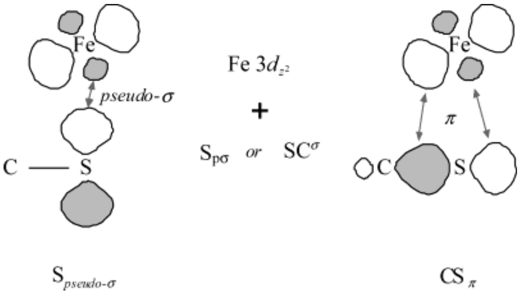

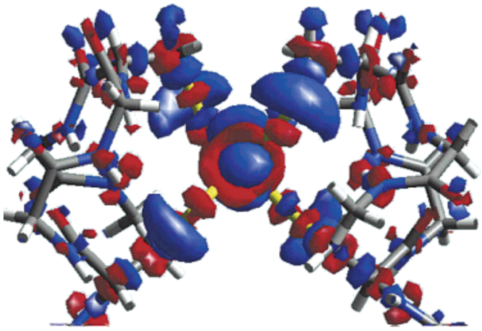

Figure 5. DFT-calculated redox density (ρ_{redox}) for the oxidation of *Desulfovibrio vulgaris* Rubredoxin (1RB9). Surfaces are generated using a ±0.01 e/Å^2 cutoff where red (loss) and blue (gain) surfaces represent the net change of electron density upon oxidation.

dominated by Fe 3d$_{z^2}$ character (~85%) with only minor contributions from each cysteinate ligand.[50]

The DFT-calculated molecular axis coincides with that obtained from single-crystal spectroscopic data.[51,52] The Fe 3d$_{z^2}$ orbital is oriented away from the protein surface, and its major electron density is encapsulated by the side chains of Val(8), Tyr(11), Val(41), and Ala(44) (see Figure 4B).[53] Ligand contributions to the RAMO come from two distinct cysteinate fragment molecular orbitals (FMOs); these are shown in Scheme 1. The higher-energy FMO is termed the $S_{\text{pseudo}-\sigma}$ and is essentially an isolated S 3p orbital (perpendicular to the S−C bond) that interacts in a pseudo-σ manner with the Fe 3d$_{z^2}$ orbital. Its pseudo-σ interaction with the Fe 3d$_{z^2}$ orbital results from the misdirection of the σ-orbital because the FeSC angle is >90°.[16,17]

Only this S 3p pseudo-σ FMO has previously been considered to contribute to the RAMO of Rd. However a breakdown of the RAMO contributions (Table 6) indicates that the C−S σ-bond, at deeper energy, contributes more strongly. The CS$_{\sigma}$ FMO mostly involves the S 3p orbital that forms a σ-bond with the α-carbon of the cysteinate ligand, as shown in Scheme 1; this FMO forms a π-interaction with the Fe 3d$_{z^2}$ orbital. The ligand pseudo-σ contribution to the RAMO was previously evaluated by analysis of a weak low-energy S → Fe 3d$_{z^2}$ charge-transfer transition; that analysis indicated ~4−5% ligand character in the RAMO. The additional contribution from SC$_{\pi}^{\sigma}$ could not be evaluated spectroscopically as the associated CT transition would be at high energy. When both ligand contributions are included, the overall ligand character in the RAMO increases to ~14%. The asymmetry at the active site from the Cys$_a$ and Cys$_b$ ligand sets causes a slight bias in ligand character in favor of the surface Cys$_a$ ligands (4% per Cys$_a$ ligand vs 3% for Cys$_b$). The RAMO is affected by the hydrogen bonds in a way similar to the overall electronic structure (CWT vs CEM in Table 6): the lower donor strength of the H-bonded cysteinate sulfur atoms decreases the covalency of the Fe−S interaction and the ligand character in the RAMO. The effect of electronic relaxation on CWT is also similar to that previously observed in small-molecule [Fe(SR)$_4$]$^{2-,1-}$ systems in part 1.[21] Without relaxation, the ionization process corresponds to removal of an electron from the RAMO, and the electron density change upon ionization (the redox density) corresponds directly to the square of the RAMO wave function [$\rho^*_{\text{redox}} = (\Psi_{\text{RAMO}})^2$]. Ψ_{RAMO} is depicted in Figure 4 and would constitute a predominantly metal-based redox process (see the description of the RAMO in Table 6). The inclusion of electronic relaxation significantly changes the redox density (ρ_{redox}, Figure 5). The differences between ρ^*_{redox} and ρ_{redox} (Figures 4 and 5) can be quantified by using the Mulliken decomposition scheme. This MO breakdown, provided as Supporting Information, is consistent

---

(50) The nature of the RAMO is highly dependent on the orientation of the thiolate ligands, specifically, the orientation of the α-C. Therefore, in certain model systems, the 3d$_{x^2-y^2}$ orbital is lowest in energy and becomes the RAMO.

(51) Eaton, W. A.; Lovenberg, W. *J. Am. Chem. Soc.* **1970**, *92*, 7195.

(52) Eaton, W. A.; Lovenberg, W. In *Iron−Sulfur Proteins*; Academic Press: New York, 1973; Vol. II, pp 131−162.

(53) The RAMO was considered to point towards the surface of the protein in ref 18. The full calculation of the active-site region provides the correct orientation of the RAMO with respect to the protein structure.

Table 7. Calculated Using the Method of Newton et al.[43−49]

system		$(\alpha'_L)^2$ [a]	H'^0_{DA} [b]	S_{ab} [c]	H^0_{DA} [d]
$[Fe(OH_2)_6]^{2+,3+}$	O_h	0.4%	25	0.90	23
$[Fe(SCH_3)_4]^{2-,1-}$	D_{2d}	4.1%	238	0.80	190
CWT(1RB9)	Cys_{avg}	3.5%	203	0.79	159
	Cys_a	4.3%	250	0.79	195

[a] Oxidized (α'^2_L) ligand contributions to the RAMO are shown. [b] H'^0_{DA} is the one-electron matrix element, calculated from $(\alpha'_L)^2$. [c] Passive electron overlap term (S_{ab}) calculated using the method of corresponding orbitals. [d] True electron-transfer matrix element (H^0_{DA}).

with that observed in $[Fe(SCH_3)_4]^{2-,1-}$ in part 1;[21] major changes in the passive electrons involved in Fe−S bonding lead to net oxidation on the ligands.

Calculation of H^0_{DA}. The above description of the RAMO can be used to calculate the one-electron ET matrix element, H'^0_{DA}, for direct electron self-exchange between two Rd active sites. H'^0_{DA} is calculated by using a formalism developed by Newton and co-workers[43−49] that applies McConnell's superexchange model for ET and correlates ligand contributions in the RAMO with H'^0_{DA}. Using $[Fe(H_2O)_6]^{2+}$ as a reference, H'^0_{DA} is calculated for each of the ligands assuming direct ligand−ligand contact between the redox partners. The results from extending the Newton analysis are given in Table 7. The H'^0_{DA} values for $[Fe(SCH_3)_4]^{2-,1-}$ and CWT (using Cys_{avg}) are quite similar at ∼200 cm^{-1}. Because CWT is asymmetric, H'^0_{DA} for Cys_a is somewhat larger, giving H'^0_{DA} ∼250 cm^{-1}. Calculation of the one-electron H'^0_{DA} value for $[FeCl_4]^{2-,1-}$ is complicated by the fact that the HOMO of the reduced species and the LUMO of the oxidized species are quite different; the coupling is broadly estimated at ∼200−350 cm^{-1} on the basis of the DFT results.

The influence of electronic relaxation on the ET matrix element was also developed by Newton; its effect was shown to decrease H'^0_{DA} as a result of nonunity overlap of the passive MOs of the reduced and oxidized states. The true H^0_{DA} is defined as the product of H'^0_{DA} and the passive overlap term, S_{DA}. S_{DA} is determined by using the method of corresponding orbitals whereby the overlap matrix for the reduced and oxidized states is diagonalized for the complete set of filled MOs. The method provides a quantitative evaluation of the difference between ρ^*_{redox} and ρ_{redox}. Application of this methodology allows for the calculation of a relaxation correction term for CWT ($S_{DA} = 0.787$), giving a total electronic coupling term of $H^0_{DA} \approx 200$ cm^{-1} (for Cys_a). The effect of electronic relaxation on H'^0_{DA} for CWT is very similar to that for $[Fe(SCH_3)_4]^{2-,1-}$ ($S_{DA} = 0.79$) and slightly larger than that for $[FeCl_4]^{2-}$ ($S_{DA} = 0.82$), in good agreement with the Δq_{rlx} values observed in part 1.

Electron-Transfer Pathways in Rubredoxin. For Rd, any evaluation of the effects of electronic relaxation on rates of electron self-exchange must take into account the fact that direct overlap of the active sites is highly improbable. As a result, it is necessary to investigate possible pathways for electron transfer through the protein matrix to the surface of the protein, where ET to its redox partner can occur. Rigorous calculations of such pathways can be performed, but to estimate relative efficiencies and define chemical pathways, a simple Beratan−Onuchic model[54] is employed to estimate the propagation of electron-transfer processes through the protein matrix. The method, which has been shown to give generally reasonable results, allows for the application of appropriate dampening factors (ϵ) to H^0_{DA} as given in eq 3, where ϵ_c, ϵ_h, and ϵ_s correspond to covalent, H-bonding, and through-space steps through the protein matrix, respectively. The variables l, m, and n correspond to the number of such steps in the total pathway through the bimolecular encounter complex.

$$H^{ij}_{DA} = H^0_{DA}\epsilon_{eff} \quad \text{where} \quad \epsilon_{eff} = \prod_l \epsilon_s \prod_m \epsilon_h \prod_n \epsilon_c \tag{3}$$

The bimolecular ET process can be treated as the product of two component paths: the path to the surface from the donor and the path from the surface to the acceptor. Further, the protein surface can be divided into different surface regions R_n, where n represents the shortest route from the active site to the surface in terms of effective σ-bonds such that $\epsilon_{eff} \approx (\epsilon_c)^n$. The above methodology generates a surface coupling map of the protein (Figure 6) that defines the different regions that should have similar coupling characteristics in the ET process. The brightly colored regions correspond to areas near the active site. The resulting data are shown in Table 8, where the fractional active surface area ($\sigma^{R_n}_{active}$) of each region is the ratio of the surface occupied by the region to the total surface area. As expected, the active site has only minimal surface exposure (0.4%) and those regions closest to the active site (R_1−R_3) correspond to only 3.2% of the total surface area of the protein. In the special case of electron self-exchange at infinite ionic strength (k^{∞}_{ese}), $\sigma^{R_n}_{active}$ represents a useful parameter for the determination of relative collisional frequencies ($\nu^{R_n\rightarrow R_m}_{rel}$), i.e., the probability that a particular R_n−R_m collision will occur. This approach allows the electron-transfer problem to be considered as the integration over all $D(R_n) \rightarrow A(R_m)$ pathways, which are each defined by a coupling element ($H^{R_n\rightarrow R_m}_{DA}$) and a relative frequency ($\nu^{R_n\rightarrow R_m}_{rel}$). $H^{R_n\rightarrow R_m}_{DA}$ is simply calculated as the product of component dampening terms and H^0_{DA}. For k^{∞}_{ese}, $\nu^{R_n\rightarrow R_m}_{rel}$ is simply the product of the fractional surface areas for the donor and acceptor surfaces: $\nu^{R_n\leftrightarrow R_m}_{rel} = \sigma^{R_n}_{active}\ \sigma^{R_m}_{active}$.

To calculate the relative importance of the different $D(R_n)$-$\rightarrow A(R_m)$ pathways using the Marcus−Hush formalism, a few additional factors need to be considered. The rate equation based on the surface regions approach is given by

$$k_{ese} = \sum_{n=0}^{n\rightarrow\infty} \sum_{m=0}^{m\rightarrow\infty} \nu^{R_n\rightarrow R_m}_{eff}\ \kappa^{R_n\rightarrow R_m}_{el}\ T^{R_n\rightarrow R_m}_{act} \tag{4}$$

The three terms are as follows: $\nu^{R_n\rightarrow R_m}_{eff}$ is the collisional frequency term ($\nu^{R_n\leftrightarrow R_m}_{eff} = \nu_c \nu^{R_n\leftrightarrow R_m}_{rel}$), $\kappa^{R_n\rightarrow R_m}_{el}$ is the transmission coefficient, and $T^{R_n\rightarrow R_m}_{act}$ is the activation term. The collisional term is simply the product of the relative

---

(54) Beratan, D. N.; Betts, J. N.; Onuchic, J. N. *Science* **1991**, *252*, 1285−1288.

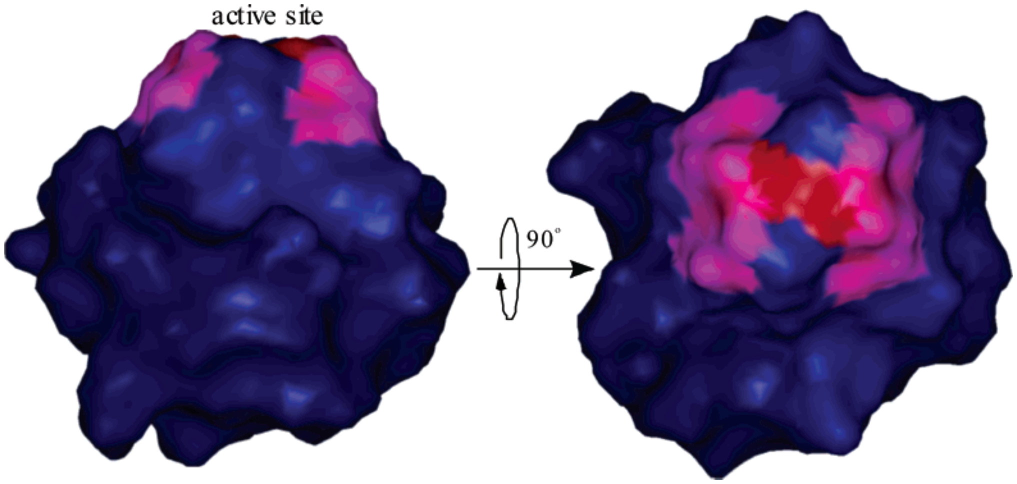

Figure 6. Surface coupling map of *Desulfovibrio vulgaris* Rubredoxin. Map of distance, in σ-bonds, of surface atoms from active site superimposed on a 4-Å solvent accessibility surface. The Beratan−Onuchic model was applied to define the σ-bond pathways from the active site to surface-accessible atoms. Results for reduced *Desulfovibrio vulgaris* Rd (1RB9) are shown. MSI Inc. Cerius^2 and WebLab Viewer Pro software were used to define surfaces and visualize the results. For visualization, active surface regions R_6−R_{9+} were condensed together.

Table 8. Fractional Active Surface Areas ($\sigma_{\text{active}}^{R_n}$) for Each Surface Region of *Dv* Rd

region	$\sigma_{\text{active}}^{R_n}$	$\epsilon_{\text{eff}}^{R_n}$
R_0	0.004	1.000
R_1	0.007	0.600
R_2	0.009	0.360
R_3	0.016	0.216
R_4	0.068	0.130
R_5	0.028	0.078
R_6	0.059	0.047
R_7	0.029	0.028
R_8	0.346	0.017
R_{9+}	0.435	0.010

collisional term ($\nu_{\text{rel}}^{R_n\rightarrow R_m}$, vide supra) and the average collisional frequency of protein molecules in solution ($\nu_{\text{eff}}^{R_n\leftrightarrow R_m} = \nu_c\nu_{\text{rel}}^{R_n\leftrightarrow R_m}$). Because ν_c is the same for all pathways, its value does not impact the calculation of relative rate constants. The activation term for electron self-exchange is simply $T_{\text{act}} = e^{-\lambda 4RT}$, and it is also independent of the pathway, assuming that the total reorganization energy for electron transfer is similar for all component pathways. The final term is the transmission coefficient, which is a function of both λ and $H_{\text{DA}}^{R_n\rightarrow R_m}$.

The Landau−Zener formulation is used to calculate $\kappa_{\text{el}}^{R_n\rightarrow R_m}$ (see eq 5).[47] Other formulations are available, including some that are not explicitly defined for nonadiabatic processes,[55−63] but the Landau−Zener formulation is reasonable for estimating $\kappa_{\text{el}}^{R_n\rightarrow R_m}$ for a range of different $H_{\text{DA}}^{R_n\rightarrow R_m}$ values for ET processes that are not solvent-limited. To calculate $\kappa_{\text{el}}^{R_n\rightarrow R_m}$, it is necessary to obtain a reasonable estimate of λ as $H_{\text{DA}}^{R_n\rightarrow R_m}$.

$$\kappa_{\text{el}}^{R_n\rightarrow R_m} = \frac{2P_0}{1+P_0} \quad \text{where}$$

$$P_0 = 1 - \exp\left[\frac{-(H_{\text{DA}}^{\text{R}_n\rightarrow \text{R}_m})^2}{h\nu_n}\left(\frac{\pi^3 RT}{\lambda}\right)^{1/2}\right] \quad (5)$$

Earlier, a value of $\lambda_{\text{i}}^{\text{ese}}$ was calculated for the gas-phase electron self-exchange for $[\text{Fe(SCH}_3)_4]^{2-,1-}$ at 0.12 eV. For the larger CWT model, $\lambda_{\text{e}}^{\text{se}}$ has been calculated from the Opt-Red → Opt-Ox structures, giving $\lambda_{\text{i}}^{\text{ese}} = 0.2$ eV. These values are in reasonable agreement with experimental and theoretical estimates for $[\text{Fe(SR)}_4]^{2-,1-}$ model systems and for Rd ($\lambda_{\text{i}}^{\text{ese}} \approx 0.3$ eV).[3,26,64−68] Some experimental kinetic data are available from which the outer-sphere reorganization energy can be roughly estimated.[27,28] Additionally, literature estimates for biological ET processes generally suggest that 0.4 eV $\leq \lambda_{\text{o}}^{\text{ese}} \leq$ 0.7 eV is a reasonable estimate for Rd.[69,70] We thus use 0.7 eV as a lower estimate of λ^{ese} for Rd.

Generally, biological ET processes are nonadiabatic, i.e., $\kappa_{\text{el}} \ll 1$, where the transition probability for ET is very low. We can calculate $\kappa_{\text{el}}^{R_0\rightarrow R_0}$ from eq 5 using $\lambda^{\text{ese}} = 0.7$ eV and $H_{\text{DA}}^{R_0\rightarrow R_0} = H_{\text{DA}}^0 = 250\ \text{cm}^{-1}$, yielding $\kappa_{\text{el}} \approx 0.5$. The result is robust to a wide range of λ^{ese} values, as demonstrated in

---

(55) Tominaga, K.; Walker, G. C.; Kang, T. J.; Barbara, P. F.; Fonseca, T. *J. Phys. Chem.* **1991**, *95*, 10485−10492.

(56) Raineri, F. O.; Friedman, H. L. In *Electron Transfer*−*From Isolated Molecules to Biomolecules*; John Wiley & Sons, Inc: New York, 1999; Vol. 107, Part 2, pp 81−189.

(57) Basilevsky, M. V.; Parsons, D. F.; Vener, M. V. *J. Chem. Phys.* **1998**, *108*, 1103−1114.

(58) Yoshihara, K.; Nagasawa, Y.; Yartsev, A.; Johnson, A. E.; Tominaga, K. *J. Mol. Liq.* **1995**, *65*−*6*, 59−64.

(59) Yoshihara, K.; Tominaga, K.; Nagasawa, Y. *Bull. Chem. Soc. Jpn.* **1995**, *68*, 696−712.

(60) Rips, I.; Jortner, J. *Jerusalem Symp. Quantum Chem. Biochem.* **1990**, *22*, 293−299.

(61) Rips, I.; Klafter, J.; Jortner, J. *J. Phys. Chem.* **1990**, *94*, 8557−8561.

(62) Rips, I.; Klafter, J.; Jortner, J. *Photochem. Energy Convers., Proc. Int. Conf. Photochem. Convers. Storage Solar Energy, 7th* **1989**, 1−22.

(63) Rips, I.; Jortner, J. *Chem. Phys. Lett.* **1987**, *133*, 411−414.

(64) Sigfridsson, E.; Olsson, M. H. M.; Ryde, U. *Inorg. Chem.* **2001**, *40*, 2509−2519.

(65) Cambray, J.; Lane, R. W.; Wedd, A. G.; Johnson, R. W.; Holm, R. H. *Inorg. Chem.* **1977**, *16*, 2565−2571.

(66) Lane, R. W.; Ibers, J. A.; Frankel, R. B.; Holm, R. H. *Proc. Natl. Acad. Sci. U.S.A.* **1975**, *72*, 2868−2872.

(67) Lane, R. W.; Ibers, J. A.; Frankel, R. B.; Papaefthymiou, G. C.; Holm, R. H. *J. Am. Chem. Soc.* **1977**, *99*, 84−98.

(68) Papaefthymiou, G.; Frankel, R. B.; Lane, R. W.; Holm, R. H. *Bull. Am. Phys. Soc.* **1976**, *21*, 317−317.

(69) Blankman, J. I.; Shahzad, N.; Miller, C. J.; Guiles, R. D. *Biochemistry* **2000**, *39*, 14806−14812.

(70) Fraga, E.; Webb, M. A.; Loppnow, G. R. *J. Phys. Chem.* **1996**, *100*, 3278−3287.

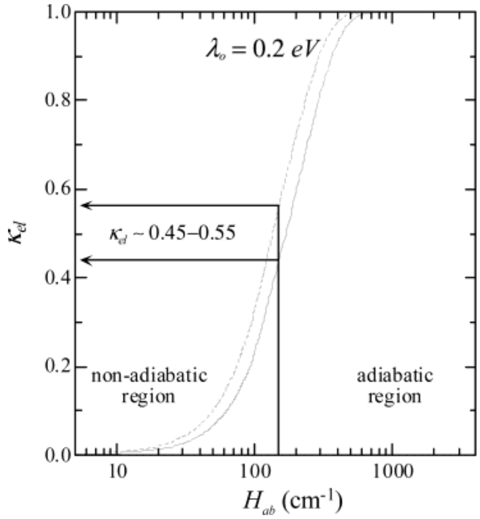

Figure 7. Electron transmission coefficient ($\kappa_{\mathrm{el}}^{\mathrm{ese}}$) as a function of calculated $H_{\mathrm{ab}}^{\mathrm{ese}}$ for two limiting values of $\lambda_{\mathrm{o}}^{\mathrm{se}}$ based on other systems.

Table 9. κ_{el} (%) Calculated for Specific Self-Exchange Pathways[a] Assuming $\lambda^{\mathrm{ese}} = 0.7$ eV

donor regions	acceptor regions				
	R_0	R_1	R_2	R_3	R_4
R_0	0.47	0.22	0.09	0.03	0.01
R_1	–	0.09	0.03	0.01	*
R_2	–	–	0.01	*	*
R_3	–	–	–	*	*
R_4	–	–	–	–	*

[a] All terms labeled with * are pathways where $\kappa_{\mathrm{el}} \ll 0.01$.

Table 10. Breakdown of Surface Region[a] Contributions to the Rate of Electron Self-Exchange of Rubredoxin as a Percentage of the Total Calculated Rate Constant

donor regions	acceptor regions									
	R_0	R_1	R_2	R_3	R_4	R_5	R_6	R_7	R_8	R_{9+}
R_0	8.5	10.1	3.8	2.7	4.1	0.6	0.5	0.1	0.4	0.1
R_1		10.9	3.8	2.6	4.0	0.6	0.5	0.1	0.3	0.1
R_2			1.3	0.8	1.3	0.2	0.1	–	0.1	–
R_3				0.6	0.9	0.1	0.1	–	0.1	–
R_4					1.3	0.2	0.1	–	0.1	–
R_6							–	–	–	–
R_7								–	–	–
R_8									–	–
R_{9+}										–

[a] Region R_0 corresponds to the [Fe(SC)$_4$] moiety. The subsequent regions, R_n, are each defined for active surface regions that correspond to n σ-bonds from R_0, except for the final region, R_{9+}, which includes the complete active surface for $n > 8$. The final column designates the sum of contributions for the interactions of a specific region on the donor over the complete surface of the acceptor.

Figure 7, which suggests that *direct* Rd self-exchange would be nearly adiabatic. $\kappa_{\mathrm{el}}^{R_n \rightarrow R_m}$ can be calculated for all $D(R_n) \rightarrow A(R_m)$ pathways by using the appropriate $H_{\mathrm{DA}}^{R_n \rightarrow R_m}$ based on the effective dampening factor for the donor-to-acceptor pathway under consideration. Table 9 lists $\kappa_{\mathrm{el}}^{R_n \rightarrow R_m}$ values for all $D(R_n) \rightarrow A(R_m)$ pathways.

From Table 9 and $\nu_{\mathrm{el}}^{R_n \rightarrow R_m}$, the relative importance of each pathway can be determined. The results of this analysis are given in Table 10. An informative way of considering these results is presented in Figure 8, where the sums of contributions of all $D(R_0{-}R_n) \rightarrow A(R_0{-}R_n)$ pathways are systematically included in the total analysis. Thus, we see that R_0 and R_1 together should account for ~40% of the total rate. Inclusion of pathways up to R_4 accounts for ~90% of the total self-exchange rate even though these pathways account for only 10% of the total surface area. These results demonstrate that regions where $n \geq 5$ (see blue regions in Figure 6) will likely contribute little to $k_{\mathrm{ese}}^{\infty}$ even though they include the majority of the surface area of the protein.

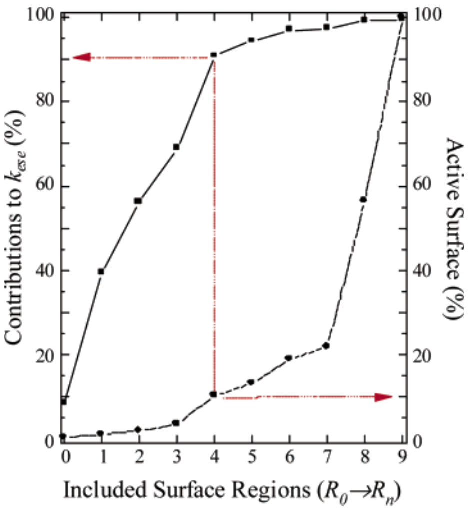

Figure 8. Contributions to total calculated rate of electron self-exchange for rubredoxin as a function of active surface regions included in the analysis. Each $R_0{-}R_n$ region corresponds to the total contribution of all regions in that range for both the donor and the acceptor. The protein surface is defined using a 4-Å solvent surface map for structure 1RB9.

This analysis further allows for the determination of which pathways specifically contribute to electron self-exchange. Regions R_0 and R_1 both involve superexchange through the $-$SCH$_2-$ moiety of Cys$_{\mathrm{a}}$, the cysteinate ligands that lie closest to the surface of the protein. This is the shortest path to the surface, but it represents only 1% of the total protein surface ($\sigma_{\mathrm{active}}^{R_0+R_1} \approx 0.011$, Table 8). The β-methylene protons provide the greatest accessible surface area and contribute significantly to these pathways. Regions R_2 and R_3 correspond to progressions along the Cys$_{\mathrm{a}}$ residues with contributions from C(α) and its proton, as well as other backbone atoms. The surface area for these two surface regions is still very small, accounting for only 2.5% of the total surface. The surface area for R_4 accounts for nearly 7% of the total surface area and corresponds to surface-exposed backbone amide oxygens from Thr(7), Val(8), Gly(10), Pro(40), Val(41), and Gly(43). The importance of these paths is significant mostly by virtue of their large surface accessibility as well as the fact that each of these pathways is connected to the active site directly through hydrogen bonds (OCNH···S) to the cysteinate ligands. For regions further from the active site than $n \geq 5$, the active surface area remains small until very long distances ($n \geq 8$) while the transmission coefficient continues to decrease substantially. The influence of these longer pathways is therefore quite small.

Effect of Electronic Relaxation on ET Rates. The analysis applied above can easily be used to determine the relative influence of electronic relaxation on the overall rates of electron self-exchange for $[FeCl_4]^{2-,1-}$, $[Fe(SCH_3)_4]^{2-,1-}$, and Rd; the effects are very similar in all cases. In each system, electronic relaxation significantly decreases the inner-sphere reorganization energy and slightly decreases the electronic coupling matrix element. Whereas the former effect should increase the rate, the latter has the opposite effect. On the whole, however, the effect is dominated by the nearly 1 eV decrease in λ_i^{ese}. Irrespective of contributions from specific pathways in Rd, the decrease in λ_e^{se} results in an increase in the overall rate of electron self-exchange by 3 orders of magnitude, providing dramatic evidence for the importance of electronic relaxation in defining the electron-transfer properties of iron−sulfur active sites

Discussion

Our investigations of electronic structure contributions to the kinetics of electron self-exchange for Rd provide significant insight into the overall factors that affect its reactivity. In accordance with other studies on the ET properties of tetrathiolate iron complexes, the electronic structure of the reduced site changes dramatically upon oxidation. We have evaluated the importance of these electronic structure effects on both λ_e^{se} and H_{DA} and their impact on electron-transfer reactivity. Overall, electronic relaxation is found to play an important role in determining the electron-transfer kinetics of both $[FeCl_4]^{2-,1-}$ and $[Fe(SR)_4]^{2-,1-}$ systems.

The small inner-sphere reorganization energies for tetrathiolates are inherent to these complexes because of their small Δr_{redox} values in contrast to $[FeCl_4]^{2-,1-}$, where Δr_{redox} and thus λ_i^{ese} are significantly larger. Bond distance changes are effectively governed by Δq_{redox}, the change in the charge on the metal upon redox. Importantly, Δq_{redox} can be experimentally determined from core ionization energies obtained by XPS. From these studies, we find that $[Fe(SCH_3)_4]^{2-,1-}$ has a small λ_e^{se} because its Δq_{redox} is very small ($\sim 0.1\bar{e}$) in contrast to $[FeCl_4]^{2-,1-}$, which has a significantly larger λ_i^{ese} and Δq_{redox} values. The potential energy surfaces in Figure 2 provide insight into the factors that control these differences and, by extension, the inner-sphere reorganization energy. The effect can be interpreted by defining a linear distorting force ($\partial V/\partial r$) upon ionization of the reduced species. This distorting force correlates with the increased electrostatic attraction between the metal and ligands upon oxidation. Differences in both the initial electronic structure (nature of the RAMO) and electronic relaxation result in the observed differences in $\partial V/\partial r$ that act on the two reduced complexes upon oxidation. The greater covalency of the tetrathiolate and its larger electronic relaxation (relative to the tetrachloride) both contribute in decreasing Δq_{redox} and thus $\partial V/\partial r$, resulting in a small Δr_{redox} and λ_i^{ese}.[71] As a result, the inner-sphere reorganization energy of the tetrathiolate redox couple is well-tuned for rapid electron transfer. Importantly, electronic relaxation has a dramatic influence on λ_i^{ese} for *both* redox couples, decreasing each by almost 1 eV as a result of the dramatic charge redistribution that minimizes $\partial V/\partial r$ for contraction of the M−L bonds.

With respect to H_{DA}, the orientation of the RAMO relative to the surface of the protein negates the possibility of direct metal−metal contact as a primary pathway for electron transfer.[53] Electron transfer must therefore occur through superexchange from the iron to its cysteinate ligands.[72] The metal-based RAMO has little ligand character for effective superexchange, but only moderate electronic coupling to the ligand is needed to obtain good transmission through to the cysteinate −SC− group. The one-electron electronic coupling matrix element in the absence of electronic relaxation, H'^{0}_{DA}, is determined by the amount of ligand character in the RAMO, which remains unchanged by the redox process. By contrast, the passive electrons—specifically those involved in defining the metal−ligand bonding—respond rather dramatically to the redox process. The charge redistribution in the passive orbitals upon redox lowers the electronic coupling by ∼20%, which is possibly somewhat surprising because electronic relaxation shifts so much electron density back to the metal that the overall process is mostly ligand-based (see Figure 5).

The resulting active-site electronic coupling term H^0_{DA} is $\sim 200\ cm^{-1}$, which is twice as large as previously estimated from analysis of the experimental low-energy $S \rightarrow Fe\ 3d_{z^2}$ charge-transfer transition. The DFT results indicate that the S−C σ-bond can also weakly interact with the RAMO (Scheme 1), but its CT transition is too high in energy to be experimentally observed. Its contribution must also be included in the calculation of H^0_{DA}. This ligand contribution provides a mechanism for the RAMO to interact directly with the σ-bond network of the protein.

Potential pathways for electron transfer were investigated to determine their relative importance in electron self-exchange. The ligand superexchange mechanism to the surface −SC− moieties allows for electron transfer that is near-adiabatic, but the statistical probability of creating the proper encounter complex to obtain this pathway is very small [$(\sigma^{R_0}_{active})^2 \approx 10^{-5}$, see Table 8]; for this reason, longer pathways are also found to contribute significantly. The surface regions R_0−R_4 are found to contribute to electron transfer, whereas regions at >4 effective σ-bonds from the active site (Figure 6, blue regions) should contribute very little to the rate even though they constitute the majority of the surface of the protein. The major pathways within R_0−R_4 are summarized in Figure 9. The two main pathways are superexchange through (A) the β-methylenes of the surface cysteinate ligands and (B) the sulfur H-bonds of the cysteinate sulfurs to the surface amide oxygens. The cys-

---

(71) Some additional factors further lower the distorting force in the tetrathiolate. The electrostatic charge model should be redistributed within the ligand, and the model assumes that only a single distorting mode is consequential.

(72) Recent studies have suggested that structural rearrangement of the active site could be sufficient to allow direct access to the iron. The crystallographic data used to support this proposal show a water molecule near the active site but still ∼4 Å away from the iron itself. The water is in close contact with one of the surface cysteinates and would ultimately allow for effective solvent-mediated electron transfer *through the cysteinate ligand.*

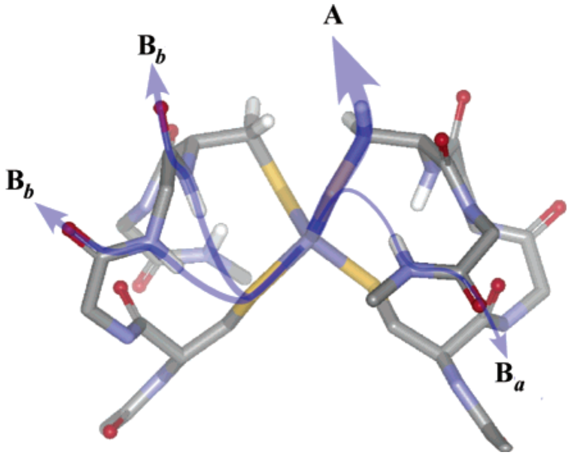

Figure 9. Electron-transfer pathways in Rd. Two major pathways contribute to the electron self-exchange in Rd*:* (A) direct superexchange to the surface cysteinates and (B) pathways involving hydrogen-bonded amide groups to both types of cysteinates.

teinate H-bonds create additional paths to the surface and significantly increase the active surface area for electron self-exchange.[73] The above analysis does not include potential solvent-mediated ET pathways.[74] However, judging from the limited range of protein-mediated pathways, rapid solvent-mediated ET could occur only within regions R_0-R_1, thus limiting the solvent-mediated pathways to those involving the proximal cysteinate side chains (Cys_a).

Final Remarks

Rd is obviously well-designed for its role in electron transport, allowing fast electron transfer in a controlled fashion. Efficient electron transfer with other proteins is limited to only a small region of the overall protein surface. “Hot spots” are the Cys(9) and Cys(42) ligands (mostly the 3-methylene groups) and the oxygens of backbone amide groups hydrogen-bonded to the S Cys ligands. Furthermore, the electronic structure of the active site itself is inherently well-designed for fast electron transfer by minimizing inner-sphere reorganization through both high covalency and very large electronic relaxation upon oxidation. The large influence of electronic relaxation, which stabilizes the oxidized state through LMCT, is found to dramatically increase the rate of electron transfer. The mostly *ligand-based* electron transfer that results from electronic relaxation still retains the fundamental character of metal-based one-electron ionization and allows for near-adiabatic ET at the active site and through a limited number of longer-range pathways.

Acknowledgment. Financial support for this research was provided by the National Science Foundation (NSF CHE-9980549). Valence PES data were obtained at the Stanford Synchrotron Radiation Laboratory (SSRL). SSRL is funded by the U.S. Department of Energy, Office of Basic Energy Sciences. Partial financial support was provided to P.K. from SSRL. Graduate fellowship support for P.K. was provided by the Natural Sciences and Engineering Research Council of Canada (NSERC/CRSNG).

Supporting Information Available: Input files and structural information for DFT calculations used in this paper. Input files for TT-Multiplets simulations. Figure showing the effect of anharmonicity. This material is available free of charge via the Internet at http://pubs.acs.org.

IC0203320

---

(73) The importance of the H-bond pathways can be seen by recalculating the rate constant using the CEM structure where the active-site H-bonds have been broken. In this case, the rate constant drops by approximately 30%.

(74) Yang, Y.; Beck, B. W.; Shenoy, V. S.; Ichiye, T. *J. Am. Chem. Soc.* **1993**, *115*, 7439−7444.